Validation of a multimodal set-up for the study of zirconium alloys claddings' behaviour under simulated LOCA conditions

Damien Campello, Nicolas Tardif, Jean Desquines, Marie-Christine Baietto, Michel Coret, Anne Maynadier, Philippe Chaudet

VALIDATION OF A MULTI-MODAL SETUP FOR THE STUDY OF ZIRCONIUM ALLOYS CLADDINGS' BEHAVIOR UNDER SIMULATED LOCA CONDITIONS

D. CAMPELLO[A], N. TARDIF[A], J. DESQUINES[B], M.-C. BAIETTO[A], M. CORET[C], A. MAYNADIER[D], P. CHAUDET[A]

[A] Univ Lyon, INSA-Lyon, CNRS UMR5259, LaMCoS, F-69621, France

[B] IRSN/PSN-RES/SEREX/LE2M, Saint Paul lez Durance, France

[C] GeM (UMR6183), Ecole Centrale de Nantes, 1 rue de la Noë 44321 Nantes, France

[D] FEMTO-ST, UMR CNRS 6174, Applied Mechanics Department, 24 rue de l'Epitaphe, 25000 Besançon, France

Corresponding author:

Nicolas Tardif

Laboratoire de Mécanique des Contacts et des Structures

Université de Lyon, CNRS, INSA-Lyon UMR5259

27 bis avenue Jean Capelle - F69621 Villeurbanne Cedex France

T. +33 (0)4 72 43 84 52

F. +33 (0)4 72 43 09 80

nicolas.tardif@insa-lyon.fr

ABSTRACT

In [2], the authors used a combined experimental / numerical approach to identify the creep behavior of as-fabricated Zircaloy-4 claddings under simulated LOCA conditions. The current paper deals with the uncertainties and errors estimation of the two key methods used to measure the thermal and kinematic full fields during the creep tests: Near Infra-Red Thermography (NIRT) and 2 Dimensional Digital Image Correlation (2D-DIC).

The NIRT uncertainties are evaluated as 0.7% of the actual temperature. They are mainly due to the thermocouple measurements used to calibrate the radiometric model of the NIRT.

A combined 2D-DIC / edge detection approach is proposed to quantify the error related to 2D-DIC when measuring the ballooning of the tubular specimen. The 2D-DIC error is evaluated as 0.1% of the actual equivalent strain even for ballooning inducing a radius increase of 20%.

Keywords: Digital Image Correlation, Near Infra-Red Thermography, uncertainties, measurement error

1   INTRODUCTION

During its operating life, the water in the primary loop of a Pressurized Water Reactor (PWR) is pressurized at 155 bar and heated by fuel pellet stacks up to 320 °C. The fuel pellets are inserted in claddings assembled in a 27x27 bundle. They are made of zirconium alloys. The claddings are designed to be the first safety barrier in French PWR. In operating lifecycle, filling gas and fission gas release also internally pressurizes the fuel claddings. A Loss of Coolant Accident scenario (LOCA) postulates a breach in the primary loop system. The water is depressurized limiting the coolant efficiency. Both the water and the fuel rods are then heated and the claddings are loaded with internal pressure. It can lead to rod ballooning and, potentially, to rod bursting. Re-flooding the nuclear core reactor interrupts this accidental sequence. The fuel rod ballooning can impede the core cooling capacity by flow blockage. The PERFROI project, detailed in [1], aims to study this complex scenario.

In [2], the authors presented the global picture of the coupled experimental/numerical approach to identify the steady-state creep behavior of as-fabricated Zircaloy-4 claddings under simulated LOCA conditions. The study targeted thermal-mechanical conditions corresponding to the lower bound of phase transformation from α towards α + β where several creep mechanisms are potentially activated (i.e. temperatures between 750 and 850 °C, stress

between 7 and 45 MPa). Fig. 1 summarizes the methodology. The experimental setup enabled the internal pressurization of an unirradiated Zircaloy-4 cladding by stage. An induction heating system induced an axisymmetric but axially heterogeneous thermal loading. Thermal and kinematic surface fields were monitored by optical full-field measurement methods during the ballooning. Hence, several thermal-mechanical conditions were studied during each experiment. The parameters of local Norton power laws were identified by Finite Element Model Updating by minimizing the difference between experimentally measured and calculated secondary creep strain rates. The approach enables a substantial reduction of the test matrix and associated discrepancies compared to other traditional setup [3-9].

Since the nineties, non-contact techniques in both kinematic and thermal fields measurements have been improved. Digital Image Correlation [10, 11] and edge detection [12] are frequently used for strain measurements in experimental mechanics. Recent improvements in algorithms (global approaches with finite element basis [13], multi-grid solver [14], Integrated-DIC [15], FEMU [16]...) allow for material behavior identification as proposed by Réthoré et al. in [17].

Infra-Red (IR) cameras are now commonly used in the field of experimental mechanics for computing thermal fields as demonstrated in [18] with Infra-Red Image Correlation or in [19] to explore the energy balance associated with high-cycle fatigue. The IR cameras remain very expensive compared to standard cameras, and do not allow for high spatial resolution. In order to avoid these drawbacks the Near Infra-Red (NIR) measurement methods have also been developed [20, 21, 22]. Their use (for the steel industry [23] for example, or a hot specimen in an aggressive environment [24]) has been greatly improved in the recent years.

This paper focuses on the validation of the experimental setup detailed in [2] and more specifically on uncertainties and error quantification of the 2 key optical full-field measurement methods applied in the test configuration: NIR Thermography (NIRT) and 2D Digital Image Correlation (2D-DIC).

First, the experimental setup is recalled. The Post-processing of NIRT and 2D-DIC are detailed. The NIRT protocol is then assessed. Finally, error made by the use of 2D-DIC to analyze the ballooning of the tubular specimen is then quantified by the comparison with a more accurate combined edge detection / 2D-DIC method.

2   EXPERIMENTAL SETUP

The homemade experimental setup is depicted in Fig. 2. The setup enabled a combined biaxial compression/internal pressurization loading of the tubular Zircaloy-4 sample. A local thermal loading was applied by induction heating. The specimen was surrounded by an enclosure to maintain an inert environment during the test. Windows were distributed over the circumference in order to enable the thermal and kinematic optical full-field measurements. Details on the setup are given in the following.

2.1 MATERIAL

The material was Stress Relieved Annealed (SRA) Zr-4 manufactured by CEZUS. The claddings in service have a 9.5 mm outer diameter, a 0.57 mm thickness and are 4 m long. The claddings were cut by an electro discharge machining into 90 mm long samples.

2.2 SPECIMEN PREPARATION

High temperature image correlation measurement requires meticulous preparation. A black undercoating (ULFALUX thermo-coating 1200 °C) was sprayed on the outer specimen surface. A white speckle was then applied using BND painting. The speckle size ranged from 10 to 120 μm (usual pixel size of the optical measurement was 9μm). A degreaser was used for removing the painting along the z direction at two circumferential positions separated by a 180 °C angle. Three type K thermocouples (⑭) were spot-welded in each of the painting free azimuth. The two wires of each thermocouple were separated using a single hole round ceramic insulator (SH-1-24). The diameter of the wires (CAB KX 04) was 0.078 mm to lower the intrusive effect of the thermocouples.

2.3 SETUP

The test specimen was connected (⑮ in Fig. 1) onto a Schenck 10kN servo-hydraulic tensile machine (①, ②) using custom grips (③) designed by Tardif et al. [24]. An enclosure (⑤) was fitted to the machine for working in an inert environment. Argon flushing (⑥, ⑦) was kept during the entire test with a constant flow.

A 6 kW induction generator (CELES) control the tube heating. The regulation was enclosed in a K-type thermocouple (⑭) measurement loop. The coils (⑨, ⑫) let a visual access to the warmest part of the specimen. The height of the region of interest (ROI, ⑬) is $z_0 = 20\ mm$. A proportional pressure regulator (IMF) linked to an argon cylinder controlled the pressurization (⑧) of the specimen. Two pressure gages (P8AP from HBM, ④) mounted onto the upper and lower grips measured the internal pressure. The pressure induced bottom-end effect was mechanically compensated by an axial compressive force F inducing a uniaxial hoop loading.

Five sapphire glasses were distributed over the enclosure to enable optical monitoring of the ROI by 4 digital cameras (⑩) equipped with 200 mm macro optics (NIK AF MICRO-NIKKOR 200MM F/4 D IF-ED).

Two 12MPx CMOS cameras (VC-12MC-M65E0-FM) performed the 2D-DIC on the tubular specimen surface at temperatures ranging from 750 to 850°C. At such temperatures, the cladding surface emits radiation in the Near Infra-Red (NIR) spectral range. To get rid of incandescence, blue LED rings (CCS LDR2-70-BL2, 470nm, ⑪) were set up above and below the induction coils. The LED rings were pulsing blue light. Band-pass filters (MIDOPT FIL BP470/62) centered on 470 nm (useful range: 425-495nm) were fitted to the 12 MegaPixels cameras used for DIC as proposed by Pan et al. in [25, 26].

Additionally, two 16MPx CCD cameras (Prosilica GE4900) shot images without any filtering when the blue lights were put off for NIRT. This way, only the light emitted by the specimen surface radiation was captured.

3   DEDICATED TEST PROCEDURES FOR ERRORS AND UNCERTAINTIES ASSESSMENT OF THE FULL FIELD MEASUREMENTS

3.1   TEST PROCEDURE TEST A FOR NIRT ASSESSMENT

A thermal cycling test was performed on a cladding at three different temperature levels. The thermal loading history is plotted versus time in Fig. 3. The cladding was first heated then three thermal cycles were successively performed and had actual both heating and cooling rates of $2.2°C.s^{-1}$. Argon flushing was kept during the whole test. The force was also set to zero. Note that the dedicated test conditions were aggravating compared to those in [2]

(isothermal creep). Radiometric models were calibrated for each cycle during its own heating part. A Prosilica GE4900 camera shot pictures at a $1\ Hz$ frequency, with a $f/11$ aperture.

The test procedure will be referred as Test A in the following.

3.2   TEST PROCEDURE TEST B FOR 2D DIC ASSESSMENT

The same test procedure as in [2] was chosen to assess the 2D-DIC. The test procedure is shown in Fig. 4. At the beginning of the test, the enclosure was filled with argon gas and flushing was kept on during the whole test. A controlled axial force of 0 N was set during the $3°C \cdot s^{-1}$ thermal ramp up to a first plateau. The first plateau enabled the evacuation of the smoke induced by the heating of the paint. Then the thermal ramp was started again up to the set point (795 °C). Then, the mechanical loading was applied by the combination of the compressive force and the internal pressure. Three mechanical plateaus were set so that the J2 equivalent strain reaches at least 4% at each plateau.

The cameras configuration is shown in Fig. 5a. Images shot by Cam 1 and Cam 2 (see 5b and 5c) were respectively dedicated to 2D-DIC and edge detection. This additional digital image analysis provided the out-of-plane displacement due to the tube ballooning.

The test procedure will be referred as Test B in the following.

4   POST-PROCESSING METHODS

4.1   NEAR INFRA-RED THERMOGRAPHY

The design of the setup was chosen to apply a 20°C heterogeneous thermal axial distribution in the ROI. This temperature distribution had a strong impact on the creep strain rates as can be seen in Fig. 1. Hence Full field thermal measurement must be preferred to local measurements such as type K thermocouples. Near-Infrared thermography is well suitable to the thermal measurement of metal at temperature higher than 750°C as it can be set up with a cheap CCD or CMOS camera. These cameras types have a higher spatial resolution than usual infrared cameras. The calibration of the radiometric model requires a reference temperature measurement provided by type K thermocouples.

4.1.1   PRINCIPLE OF RADIOMETRIC MEASUREMENTS

Any surface emits radiation (with a wavelength λ) at a given temperature T. The surface is characterized by an emissivity ($0 \leq \varepsilon\ (\lambda) \leq 1$) depending on the radiation wavelength. The total emittance $\phi_{\lambda,T}^{e}$ of this surface is estimated using its emissivity and the Planck law according to equation (1). The Planck law provides the total emittance of a black-body $\phi_{\lambda,T}^{0}$ in a hemisphere using the Planck constant h, the speed of light c and the Boltzman constant k. Note that the emissivity of a black-body is equal to 1.

$$\phi_{\lambda,T}^{e} = \varepsilon(\lambda).\phi_{\lambda,T}^{0} = \varepsilon(\lambda).\frac{2h.c^2.\lambda^{-5}}{exp\left(\dfrac{h.c}{k.\lambda.T}\right) - 1} \tag{1}$$

Meriaudeau et al. detailed the concept of a radiation thermometer (RT) in [20]. A radiometer senses the radiant flux of a target. This flux is the sum of the emitted flux $\phi_{\lambda,T}^{e}$ and a reflected flux $\phi_{\lambda,T}^{ref}$ as detailed in equation (2).

$$\begin{aligned}\phi_{\lambda,T}^{tot} &= \phi_{\lambda,T}^{e} + \phi_{\lambda,T}^{ref} \\ &= \varepsilon(\lambda).L^0(\lambda,T) + [1 - \varepsilon(\lambda)].\phi_{rec}\end{aligned} \tag{2}$$

$\phi_{\lambda,T}^{ref}$ comes from the flux $\phi_{\lambda,T}^{rec}$ that the surface receives from the surroundings. A single detector (gain K and exposure time t_i) of a digital radiometer is now considered. Its digital level output I is written in equation (3) using the spectral response of the optical system $W(\lambda)$ and the total radiant flux of the target $\phi_{\lambda,T}^{tot}$. Finaly, the radiometric model gives the relation between the Temperature and the digital level recorded by the camera.

$$I = t_i.\int W(\lambda).\phi_{\lambda,T}^{tot}d\lambda \tag{3}$$

4.1.2   CALIBRATION OF THE RADIOMETRIC MODEL DURING THE HEATING STEP

In the proposed setup, induction heating induces negligible environmental heating (enclosure, argon,...). There was no other hot object in the surroundings. Moreover, the tubular geometry cannot lead to the reflection of the specimen itself. The calculation of $\phi_{\lambda,T}^{tot}$ was simplified to the emitted flux assuming that $\phi_{\lambda,T}^{rec} = 0$.

The spectral response $W(\lambda)$ of the optical image acquisition chain combined the argon's, the sapphire's and the objectives' transmittances (respectively $\tau_{ar}(\lambda)$, $\tau_{sap}(\lambda)$, $\tau_{obj}(\lambda)$), and the detector's quantum efficiency $\eta_{det}(\lambda)$, as written in equation (4).

$$W(\lambda) = \tau_{ar}(\lambda).\tau_{sap}(\lambda).\tau_{obj}(\lambda).\eta_{det}(\lambda) \qquad (4)$$

A review of several calibration methods can be found in Rotrou et al. [28]. The radiometric model was calibrated using the thermocouples local measurements during the heating phase of each test. This method is particularly well adapted since the spectral response $W(\lambda)$ is not known. Note that the thermocouples and the NIRT acquisition were triggered at exactly the same time.

Fig. 6 shows five pictures shot during the end of the heating. The thermocouples are located on the left side of the digital images. Three digital thermocouples were numerically built, close to actual Tc. They are depicted by the blue, red and green boxes in Fig. 6. An averaged gray level intensity I_{eq} was calculated into these boxes to be correlated to the associated thermocouple measurements.

Inside the digital thermocouples, the emissivity of the surface is heterogeneous because of the speckle applied onto the specimen. In order to achieve a good sensitivity to the radiation emitted by the surface, only the brightest 30% pixel intensities were averaged for computing I_{eq}.

As detailed by Rotrou in [29], the concept of equivalent wavelength λ_{eq} is useful to analytically assess a measured temperature T_{mes} based on a digital level intensity I_{eq}. The chosen radiometric model is detailed in equation (5). The parameters K_1 and K_2 of equation (6) were calibrated using the correlation between digital and real thermocouple measurements.

$$T_{mes} = \frac{K_1}{ln\left(\frac{K_2}{I_{eq}} + 1\right)} \qquad (5)$$

$$K_1 = \frac{h.c}{k.\lambda_e} \quad K_2 = 2.\varepsilon(\lambda_e).c.\lambda_e^{-4}.W(\lambda_e).t_i \qquad (6)$$

The calibration was performed using a least squares minimization between temperature T_{mes} and averaged grey level intensity I_{eq} data.

4.2   KINEMATIC FULL FIELD MEASUREMENTS

In [2], 2D-DIC measured the creep rate distribution along the yellow line in front of the cameras as depicted in Fig 5b. The ROI (white box in Fig. 5b) was discretized by isotropic linear Q4 finite elements. Their size was 30 x 30 px^2. The ill-defined problem of the optical flow conservation was solved using a non linear least squares method relying on a finite element basis. Axial and hoop displacements were extracted from 2D-DIC results at the mesh nodes. From the gradient tensors, logarithmic strains were computed. True Von Mises equivalent creep strain was calculated over the sample surface assuming material incompressibility (equation (7)) during high temperature creep.

$$\varepsilon_{zz}^{vp} + \varepsilon_{\theta\theta}^{vp} + \varepsilon_{rr}^{vp} = 0$$

$$\varepsilon_{eq}^{vp} = \left[\frac{2}{3} \left(\varepsilon_{zz}^2 + \varepsilon_{\theta\theta}^2 + \varepsilon_{rr}^2 \right) \right]^{\frac{1}{2}} \qquad (7)$$

In Test B, a coupled edge detection / 2D-DIC approach was used to quantify the error made by the 2D-DIC during the ballooning of the specimen. The edge detection method is based on the analysis of the gray level gradient of an image. Recent improvements allow for a sub-pixel definition of a curvilinear shape position and low CPU time calculations [12]. The reference line (*i.e.* edge before loading) was defined between -8mm and +8mm of the eulerian variable Z (see Fig 5c). It was discretized by 30 elements associated to a B-spline shape functions basis.

The software used to perform 2D-DIC [30] and Edge detection [12] is called Ufreckles. It has been developed by Réthoré.

The coupled edge detection / 2D-DIC approach needs two steps. The first step allows for calibrating the intrinsic parameters of the optical system used for 2D-DIC. Then the displacements and strain measured by 2D-DIC are corrected by the out-of-plane displacements measured by the edge detection measurement.

4.2.1   CALIBRATION OF THE OPTICAL MODEL

Several authors [31, 32] reported the effect of out-of-plane motion on in-plane displacements. These displacements can be corrected as proposed by Felipe-Sesé et al. in [33] using the dedicated experiment detailed in Fig. 7. The test aimed to calibrate the initial distance between the object and the optical system d_0, and the position of the intersection between the optical axis (OA) and the detector plane $O(-d_i, x_c, y_c)$.

Cam 1 (i.e. Fig. 5a) was mounted onto a sliding caliper and was translated in order to induce in-plane displacements u_r. When sliding the caliper, the 2D-DIC measures the virtual displacement of the measured point M in the detector plane $((x_2 - x_1)\vec{x} + (y_2 - y_1)\vec{y})$. This virtual displacement depends on three parameters d_0, x_c and y_c. Considering a linearized optical system model, the virtual displacement can be deduced from system equations (8).

$$d_0.(x_1 - x_c) = (d_0 - u_r).(x_2 - x_c)$$
$$d_0.(y_1 - y_c) = (d_0 - u_r).(y_2 - y_c)$$

(8)

The optical system was translated up to a maximum amplitude $u_r = 1\ mm$ then moved back to the initial position with 0.1 mm displacement steps. Parameters are determined using a least squares minimization between the displacements calculated with the optical model and the 2D-DIC. Resulting parameters d_0, x_c and y_c were respectively identified as 613 mm, -122 px and -62 px.

The virtual strain associated to the virtual displacement is depicted as a function of the normalized in-plane displacement u_r in Fig. 8. The linearization of the optical system model is validated at least for an in-plane displacement u_r of 1mm. Note that the optical system used in these experiments is not strongly affected by the out-of-plane displacement.

4.2.2   CORRECTION OF THE CLADDING BALLOONING

Fig. 9 illustrates the description of the combined edge detection / 2D-DIC approach.

2D-DIC was performed on the Region of Interest (white box in Fig. 5b) of the pictures shot during Test B. Displacements and strains in both x and y directions of the detector plane were extracted along the yellow line.

The edge detection provided the radial displacement u_r of every point of the deformed edge (Fig. 10) in the eulerian coordinate system (Fig 5c). The resulting point Q' in the detector plane corresponding to point M' can be calculated using equation (9) where $M = \frac{d_i}{d_0}$ is the magnification of the optical system.

$$y' - y_c = \frac{M.d_0}{d_0 - u_r}.(Z - Z_c).$$

(9)

The initial position Q_0 of the deformed point Q' was determined in the detector plane using the 2D-DIC results as follows:

$$y_0 - y_c = y' - y_c - u_y(Q'), \tag{10}$$

with $u_y(Q')$, the displacement of Q measured by the 2D-DIC in the y direction of the detector plane.

The initial axial position $Z_0 - Z_c$ of the deformed point M' was finally calculated using equation (11):

$$Z_0 - Z_c = \frac{y_0 - y_c}{M} \tag{11}$$

The axial and radial displacements of each point of the yellow line during the transformation from the initial to the deformed configurations were thus determined. The logarithmic strains were calculated using deformed curvilinear positions and their associated initial positions.

5   RESULTS AND DISCUSSION

5.1   NIRT ASSESSMENT

5.1.1   UNCERTAINTIES RELATED TO THE THERMOCOUPLES MEASUREMENT

Five components were involved in the acquisition chain: a thermocouple wire, a LEMO connector, a compensation wire, a converter TEPI (BEP304 model) and a FlexTest SE controller. Each of the components is a source of error affecting the temperature uncertainties. Table 1 summarizes the manufacturers data.

TC wire	Compensation	BEP304	MTS FlexTest recorder
$0.004|T|$	$\pm 2.5°C$	$\pm 6°C$	$< 3.10^{-5}|T|$

Tab. 1: Acquisition chain uncertainties

The uncertainties induced by the BEP304 take into account the internal cold junction measurement. It has the highest influence on the temperature measurement uncertainties. This manufacturer data accounts for the heating time of the cold junction. Performing measurement once the converter behavior is stabilized can reduce the uncertainties.

A calibrator (Fluke 725 Multifunction Process Calibrator) was placed before the compensation wire for assessing errors due to the compensation wire combined with the converter. It simulated the temperature of a K-type thermocouple. Five tracks of the converter were tested. The measurements were performed after 1.5 operating hour of the converter. Temperature were imposed in a range of 720 to 880 °C temperature steps. The maximal error was 0.4% of the setting temperature, and the averaged error was 0.18%. The calibration of the NIRT relied on the thermocouple measurements. The errors related to the thermocouples acquisition chain were thus passed on the final temperature estimation.

5.1.2   TEST A : NIRT UNCERTAINTIES

The temperatures calculated using the calibrated radiometric model were compared to the thermocouples measurements during Test A (Fig. 3). .

The parameters determined using the calibration process and the silicon sensor time exposure t_i are reported in Tab. 4 for each cycle.

	Cycle 1	Cycle 2	Cycle 3
t_i (ms)	70	30	14.2
K_1 (K)	$1.60\ 10^4$	$1.66\ 10^4$	$1.67\ 10^4$
K_2 (GL)	$5.96\ 10^8$	$4.34\ 10^8$	$2.4\ 10^8$
λ_e (nm)	897	869	862

Tab. 2: Radiometric model parameters calibrated during each heating

The effective wavelength λ_e was calculated using equation (6). Note that λ_e is decreasing with increasing temperature level as expected. The Digital Thermocouple (DT) and thermocouples (TC) measurements are plotted for the second temperature level cycle in Fig. 11a. The comparison between the NIRT and the thermocouple measurements are reported in Table 3 for each cycle.

Cycle	$|\Delta T/T|_{mean}$ (%)	$|\Delta T/T|_{max}$ (%)
1	0.25	0.7
2	0.14	0.54
3	0.12	0.6

Tab. 3: Comparison between thermocouples and NIRT for each cycle

Temperatures were calculated using the three radiometric models and grey level intensities ranging from 120 to 200. Results are plotted in Fig. 11b versus the grey levels normalized by their respective time exposure. The radiometric model continuity from one calibration to another is highlighted. It was expected because of the linearity between the pixel intensity and the time exposure.

The maximal difference on the temperature prediction compared to thermocouples measurements remained lower than 0.7% when considering the entire test data.

Finally, the uncertainties estimation of the NIRT method was inherent to the thermocouples measurements and remains lower than 0.7% of the true temperature and the averaged error was 0.32% of the true temperature.

5.2   TEST B : 2D-DIC ASSESSMENT

Several aspects of the 2D-DIC measurements will be discussed in the following. First, the influence of the setup on the 2D-DIC noise will be studied at room temperature and at high temperature (respectively at markers t_A and t_B in Fig. 4). Then, the error induced by the out-of-plane displacement will be regarded at different ballooning levels (markers t_1 to t_4 in Fig. 4) by using the combined 2D-DIC/edge detection approach.

5.2.1   ANALYSIS OF THE INFLUENCE OF NOISE IN 2D DIC MEASURE

At markers t_A and t_B, (respectively at room and high temperature), Cam 1 shot 30 pictures, under a constant thermal mechanical loading, for a noise analysis purpose. A stationary spatial thermal distribution was reached at t_B.

Fig. 12a shows the Grey level histogram of the ROI (red box, 1851x301 px^2). The histogram is plotted considering all the data (i.e. the pixels grey level of all pictures associated to each marker). The first pictures of the sets t_A and t_B are also shown as an example of the effect of the heating on the speckle pattern. The heating results in a decrease of the contrast

between black and white speckles. The white speckles Grey levels diminished and were smoothed. It is worth mentioning that the test constraints induce a poor speckle pattern quality either at high or room temperature as the highest quality being a wide and uniform histogram.

2D-DIC was performed with these data sets. Fig. 12b shows the displacement histogram over the whole data sets t_A and t_B (i.e. the displacement of all the nodes of each pictures). Fig 12c and Fig. 12d depict the histograms of the strains respectively at room temperature and at high temperature. The mean values and the standard deviations of each histogram are summarized in Table 4. Note that the histograms include the DIC noise but also the physical displacements induced by the thermal mechanical loading noise (see Fig. 4). The increase of noise between room and high temperature can be explained by several reasons. The dynamic of the pictures are narrower at high temperature. Little residual smoke induced by the heating of the paint could affect the measurement. However, no mirage effect was observed presumably because of the combined effect of the induction volume heating and the argon sweeping.

	Room temperature t_A			High temperature t_B		
	Displacement [mm]	Axial strain	Hoop strain	Displacement [mm]	Axial strain	Hoop strain
Mean Value	$-1.36\ 10^{-20}$	$-3.65\ 10^{-5}$	$-3.14\ 10^{-5}$	$5.46\ 10^{-20}$	$7.15\ 10^{-5}$	$9.37\ 10^{-5}$
Standard Deviation	$1.85\ 10^{-4}$	$2.05\ 10^{-4}$	$3.49\ 10^{-4}$	$4.03\ 10^{-4}$	$4.50\ 10^{-4}$	$6.71\ 10^{-4}$

Tab. 4: 2D-DIC noises at room and high temperature

Hence, the strain uncertainty at high temperature is less than $1.0\ 10^{-4}$. The strain noise is less than $1.5\ 10^{-3}$. The identification process shown in Fig. 1 used the stationary strain rates profile along the axial position of the ROI at each mechanical loading plateau. These stationary strain rates are calculated over a Von Mises equivalent strain range that is typically higher than 0.01 and over more than 20 pictures. The strain range is far higher than the strain uncertainty. The 20 pictures are enough to smooth the noise effect.

5.2.2   CORRECTION OF THE CLADDING BALLOONING

The error of the 2D DIC measurements induced by the out-of-plane displacement is quantified in the following at different ballooning levels (markers t_1 to t_4 in Fig. 4) by using the combined 2D-DIC / edge detection approach. The marker t_4 is picked because of its extremely large ballooning state

The axial strain, calculated by 2D-DIC, and the curvilinear strain, calculated by the combined edge detection / 2D DIC approach, are plotted in Fig. 13a.

The correction effect is negligible for times $t_1 \rightarrow t_3$ but it becomes significant for time t_4 when the balloon is pronounced. After correction, the axial deformation is lowered in the middle of the specimen because of the out-of-plane displacement combined to a low curvature. The opposite phenomenon is observed at the sample regions that were no longer perpendicular to the optical axis. The in-plane projection induced an artefacted contribution to ε_{yy}.

The hoop strain levels were higher than those of axial strains. The tube curvature was not accounted for considering the low chord error induced by the Finite Element discretization of the circumference of the tube at the generator location. The hoop strains calculated using 2D-DIC were thus only corrected by subtracting the virtual strain related to the out-of-plane displacement (see Fig. 8). The 2D-DIC hoop strain and the corrected one are plotted versus the position Z in Fig. 13b. The correction is not significant in the hoop direction.

In [2], the equivalent Von Mises plastic strain was used for the FEMU based identification. The equivalent true strains were computed with and without the out-of-plane displacement correction. The error er defined in equation (12) is plotted in Fig. 13c at the 4 markers.

$$er^2 = \frac{\left(\varepsilon_{eq}^{2D} - \varepsilon_{eq}^{cor}\right)^2}{\left(\varepsilon_{eq}^{cor}\right)^2} \tag{12}$$

The error associated to the 2D-DIC was lower than 1% of the equivalent strains accounting for the out-of-plane displacement even when the balloon was pronounced.

6   CONCLUDING REMARKS

The combined experimental/numerical approach detailed in [2] for identifying the creep behavior of Fresh zirconium alloys under simulated LOCA conditions was assessed.

The paper focused on uncertainties and error quantification of the two key optical full field measurement method: NIRT and 2D-DIC.

The NIRT uncertainties mainly results from the thermocouples acquisition chain used for the calibration of the radiometric model. The physically based radiometric model tends to lower these uncertainties during the calibration by correcting the discrepancies between thermocouples. An uncertainty of 0.7% of the actual temperature was quantified.

2D-DIC measured the ballooning of the tube. A correction method is proposed to take into account the out-of plane displacement of the tube during the ballooning. The method relies on a combined 2D-DIC / edge detection approach.

Applied to the used optical system, the correction is lower than 1% of the equivalent plastic strain even for a 20% increase of radius during the ballooning, value far higher than the ones used in [2] for the identification process. However, in the test configuration, axial strains are unaccurately estimated at this strain level and must be corrected from a radius increase of 10%. The proposed approach would have been particularly necessary for anisotropy identification in multiple biaxial stress states as enables the setup.

The combined 2D-DIC / edge detection approach can be used with a single camera for axisymmetric ballooning as during the above discussed testing conditions. It simplifies the setup and test procedure compared to 3D DIC.

7   ACKNOWLEDGMENT

1
2
3
4
5
6
7
8
9
10
11
12
13
14
15
16
17
18
19
20
21
22
23
24
25
26
27
28
29
30
31
32
33
34
35
36
37
38
39
40
41
42
43
44
45
46
47
48
49
50
51
52
53
54
55
56
57
58
59
60

REFERENCES

[1] G. Repetto, et al., *16th International Topical Meeting on Nuclear Reactor Thermalhydraulics.* **2015**.

[2] D. Campello, et al., *IJSS*, **2017**, 115-116,190.

[3] F. Nagase, T. Fuketa, *J NUCL SCI TECHNOL*, **2004**, 41 (7), 723

[4] C. Bushy, K. Marsh, *Tech. Rep., Colorado Cooperative Wildlife Research Unit*, **1974**.

[5] D. Kaddour, et al., Scripta Mater, **2004**, 51 (6), 515.

[6] H. E. Rosinger, et al., *Tech Rep, Atomic Energy of Canada Limited*, **1978.**

[7] M. Réocreux, E. S. de Martinville, *NED*, **1990**, 124 (3), 363.

[8] E. Ho, S. Mac Ewen, *JOM*, **1983**, 35 (2), 25.

[9] J. H. Kim, et al., *NED*, **2004**, 234, 157.

[10] M. Sutton, et al., *IMAGE VISION COMPUT*, **1983**, 1 (3) ,133. □

[11] T. C. Chu, et al., *EXP MECH*, **1985**, 25 (3), 232. □

[12] J. Réthoré, M. François, *OPT LASER ENG*, **2014**, 52, 145. □

[13] G. Besnard, et al., *EXP MECH*, **2006**, 46 (6), 789. □

[14] J. Réthoré, et al., *COMPUT METHOD APPL M*, **2007**, 196 (49), 5016.□

[15] F. Hild, S. Roux, *Comptes Rendus Mécanique*, **2006**, 334 (1), 8. □

[16] K. T. Kavanagh, R. W. Clough, *IJSS*, **1971**, 7 (1), 11. □

[17] J. Réthoré, et al., *IJSS*, **2013**, 50 (1), 73. □

[18] A. Maynadier, et al., *EXP MECH*, **2012**, 52 (3), 241. □

[19] A. Chrysochoos, et al., *JSA*, **2008**, 43 (6), 411. □

[20] F. Meriaudeau, et al., *OPT ENG*, **1996**, 35 (12), 3470. □

[21] P. Saunders, T. Ricolfi, *TEMPMEKO*, 37, 329–334.□

[22] T. Sentenac, et al.,, *IEEE T INSTRUM MEAS*, **2003**, 52 (1), 46. □

[23] F. Meriaudeau, *IMAGE VISION COMPUT*, **2007**, 25 (7), 1124. □

[24] P. Saunders, S. Bonsey, D. White, *HTHP*, **1989**, 31 (1), 83. □

[25] N. Tardif, et al., *NED*, **2011**, 241 (3), 755. □

[26] B. Pan, et al., *MEAS SCI TECHNOL*, **2011**, 22 (1). □

[27] B. Pan, et al., *OPT LASER TECHNOL*, **2012**, 44 (1), 204. □□

[28] Y. Rotrou et al., *Quantitative Infra-Red Thermography Journal*, **2006**, 3 (1), 93. □

[29] Y. Rotrou, *Ph.D. thesis*, Ecole nationale supérieure de l'aéronautique et de l'espace, **2006**. □□

[30] J. Réthoré, *INT J NUMER METH ENG*, **2010**, 84 (6), 631. □

[31] J. Réthoré et al., *OPT LASER ENG*, **2014**, 57, 20. □

[32] M. Sutton et al., *OPT LASER ENG*, **2008**, 46 (10), 746. □

[33] L. Felipe-Sesé et al., *OPT LASER ENG*, **2014**, 52, 66. □

      □

FIG. 1: Summary of the identification process detailed in [2].

FIG. 2: Experimental setup

FIG. 3: Procedure Test A : Near Infrared Thermography assessment.

FIG. 4: Procedure Test B : 2D - DIC assessment. The dashed black lines are the setting point. The plain lines are the measurements.

FIG. 5: Procedure Test B. a) Top view of the experimental setup – position of the cameras. b) Picture of CAM1, 2D-DIC performed inside the white box, data extracted along the yellow line. c) Picture of CAM2, Edge detection performed along the white line, edge in the initial configuration.
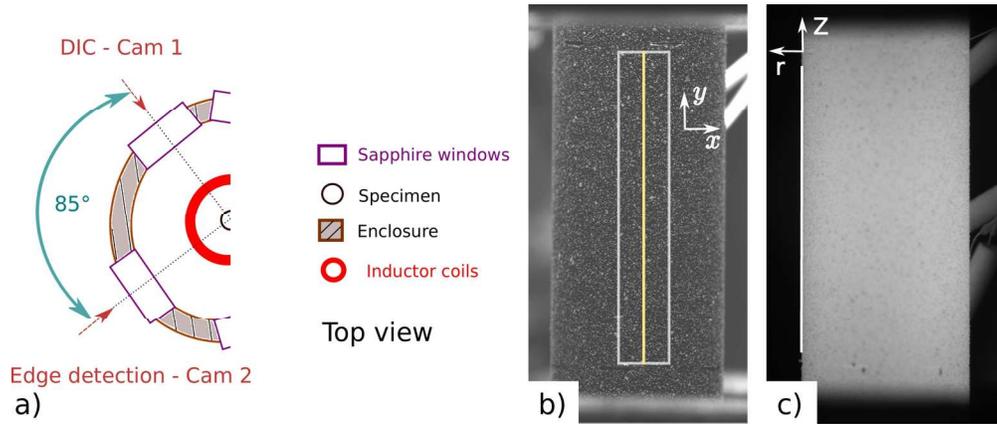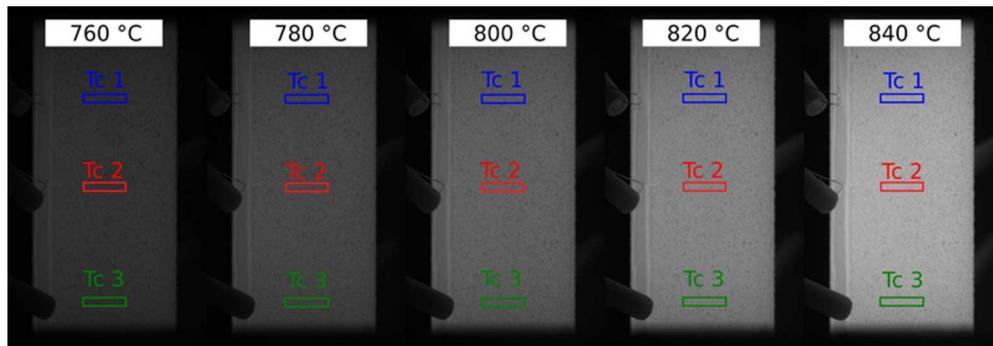
FIG. 6: Procedure Test A. Pictures shot during the end of a heating with a 850°C setting point.

FIG. 7: Procedure Test B. Scheme of the experiment used to calibrate the optical system parameters: d_0, x_c, y_c.

FIG. 8: Procedure Test B. Virtual in-plane strain versus the normalized out-of-plane displacement u_r/r_0

FIG. 9: Procedure Test B. Scheme of the combined edge detection / 2D-DIC approach.

FIG. 10: Procedure Test B. Normalized out-of-plane displacement u_r/r_0 of each marker versus the normalized axial coordinate Z/Z_0

FIG. 11: Procedure Test A a) Comparison NIRT – Thermocouples measurements for the second cycle of Test A. b) Radiometric model identification – one model per thermal cycle.

FIG. 12: Procedure Test B. a) Grey level histograms of the sets of pictures associated to markers t_A and t_B, respectively at room and high temperature (See Fig. 4). b) Displacement histograms of the sets of pictures associated to markers t_A and t_B. c) Axial (ε_{yy}) and hoop Strains (ε_{xx}) histograms related to marker t_A. d) Axial (ε_{yy}) and hoop Strains (ε_{xx}) histograms related to marker t_B.

FIG. 13: Comparison between the 2D-DIC and the combined edge detection / 2D-DIC approach, (a) axial strain, (b) hoop strain, (c) J2 equivalent strain.

FIG. 1: Summary of the identification process detailed in [2].

659x360mm (600 x 600 DPI)

1. Tensile machine
2. Load cell
3. Water cooled grips
4. Pressure sensor
5. enclosure filled with Argon
6. Low pressure argon outlet
7. Low pressure argon inlet
8. High pressure argon inlet
9. Induction power feed
10. Digital camera
11. Blue led light
12. Induction coil
13. Region of interest of the specimen : $z_0=20mm$
14. Spot welded type K thermocouples
15. Swagelok Connector
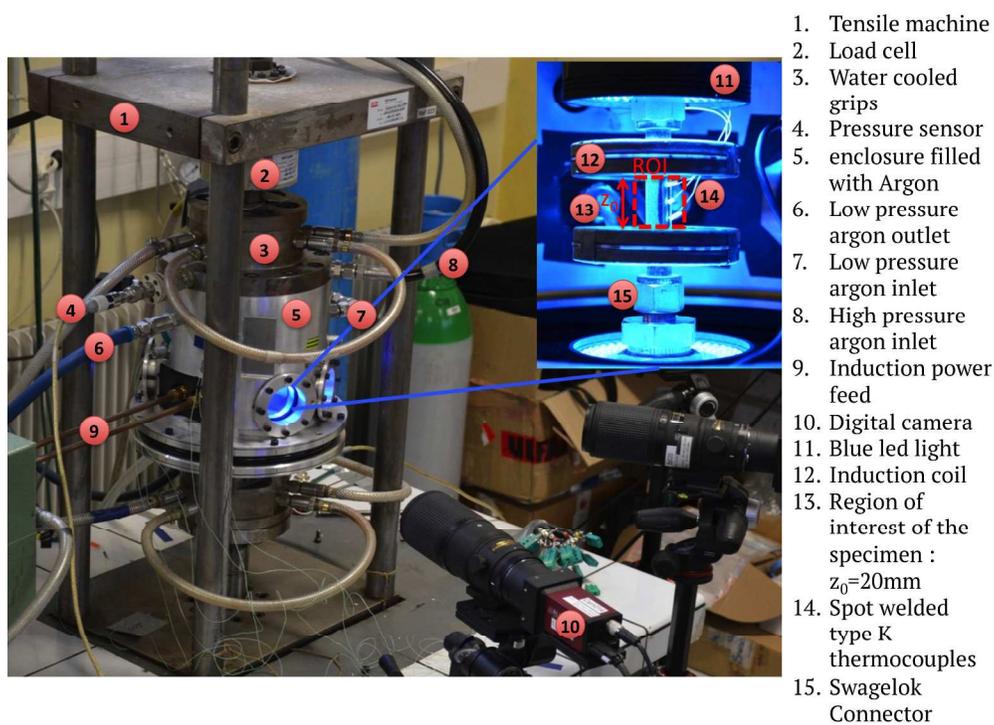
FIG. 2: Experimental setup

1057x793mm (72 x 72 DPI)

1
2
3
4
5
6
7
8
9
10
11
12
13
14
15
16
17
18
19
20
21
22
23
24
25
26
27
28
29
30
31
32
33
34
35
36
37
38
39
40
41
42
43
44
45
46
47
48
49
50
51
52
53
54
55
56
57
58
59
60
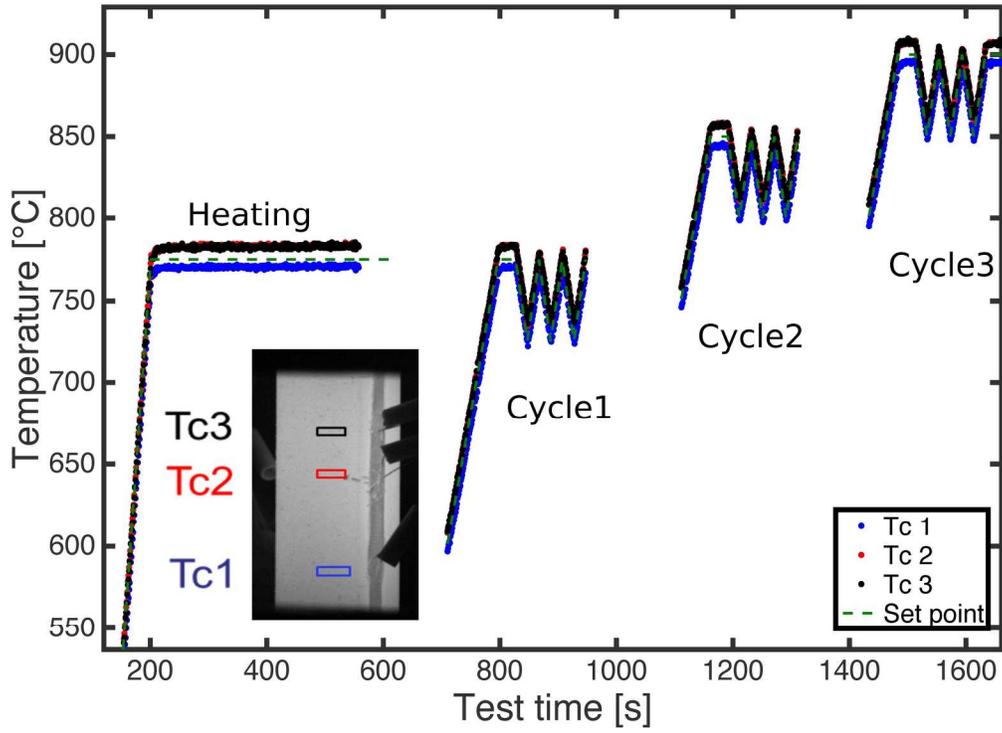
FIG. 3: Procedure Test A : Near Infrared Thermography assessment.

184x134mm (300 x 300 DPI)
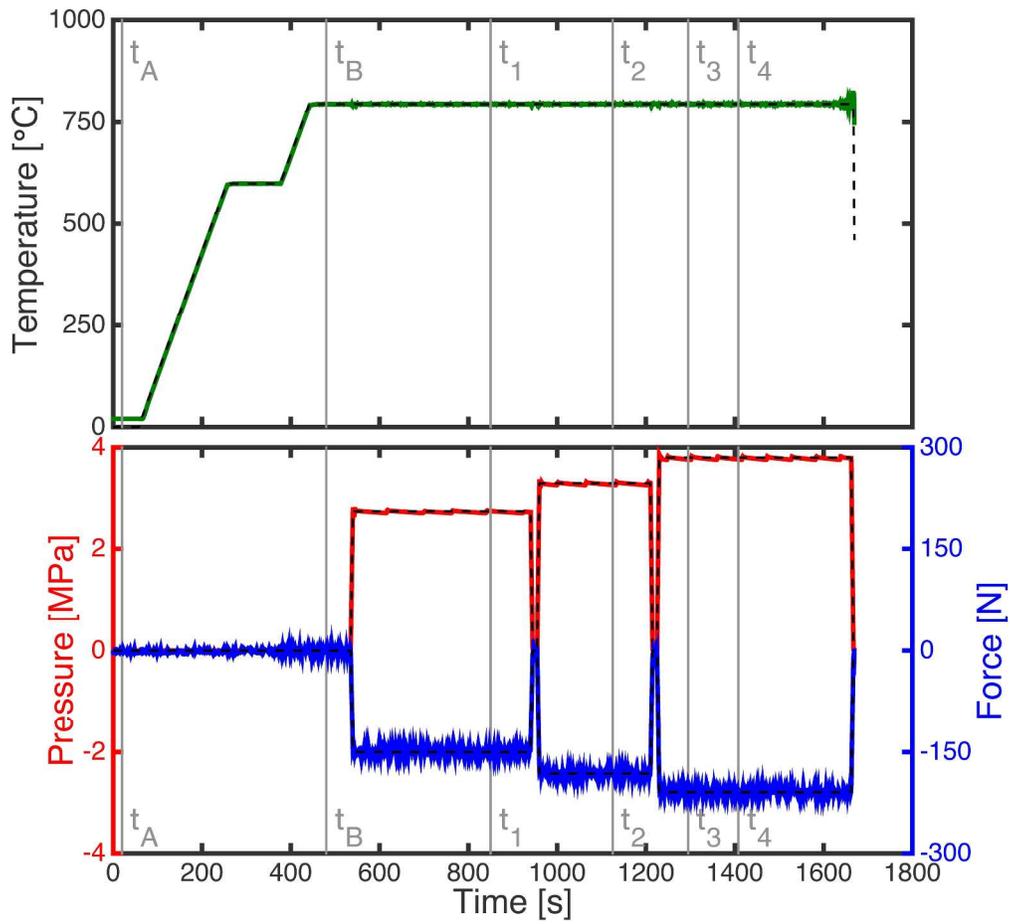
FIG. 4: Procedure Test B : 2D - DIC assessment. The dashed black lines are the setting point. The plain lines are the measurements.

286x262mm (300 x 300 DPI)

1
2
3
4
5
6
7
8
9
10
11
12
13
14
15
16
17
18
19
20
21
22
23
24
25
26
27
28
29
30
31
32
33
34
35
36
37
38
39
40
41
42
43
44
45
46
47
48
49
50
51
52
53
54
55
56
57
58
59
60

FIG. 5: Procedure Test B. a) Top view of the experimental setup – position of the cameras. b) Picture of CAM1, 2D-DIC performed inside the white box, data extracted along the yellow line. c) Picture of CAM2, Edge detection performed along the white line, edge in the initial configuration.

169x71mm (300 x 300 DPI)

FIG. 6: Procedure Test A. Pictures shot during the end of a heating with a 850°C setting point.

69x23mm (300 x 300 DPI)
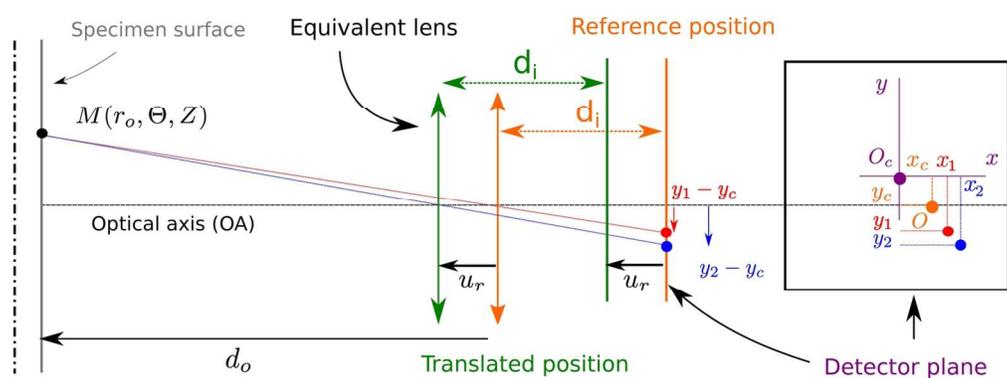
FIG. 7: Procedure Test B. Scheme of the experiment used to calibrate the optical system parameters:
d_0,x_c,y_c.

134x49mm (300 x 300 DPI)
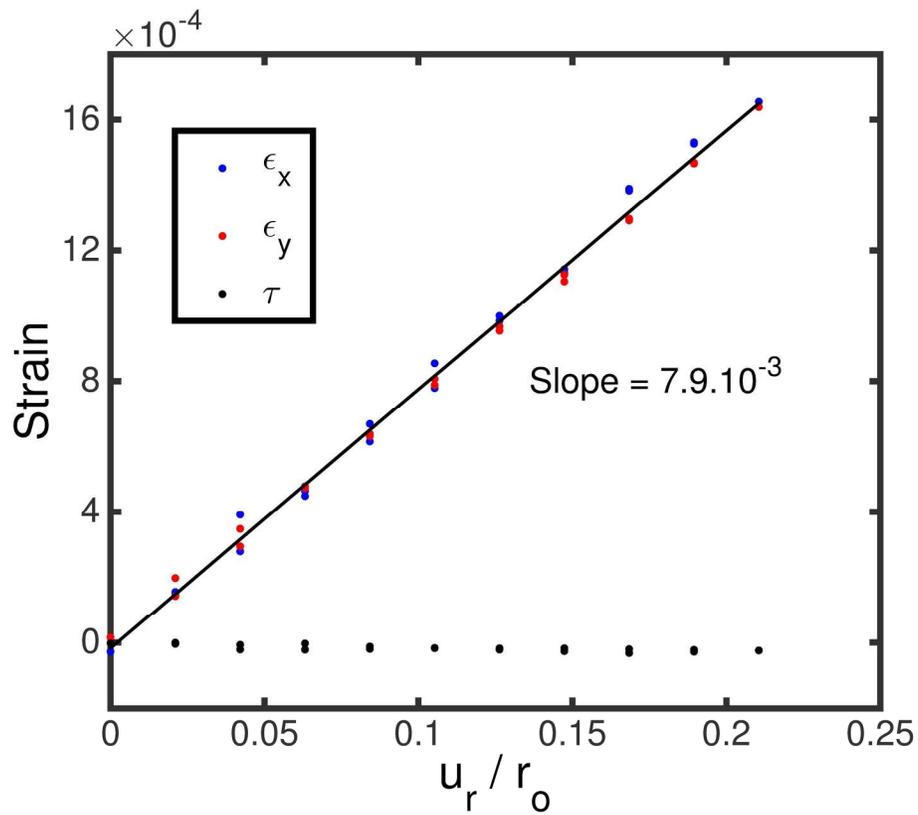
FIG. 8: Procedure Test B. Virtual in-plane strain versus the normalized out-of-plane displacement u_r/r_0

190x158mm (300 x 300 DPI)
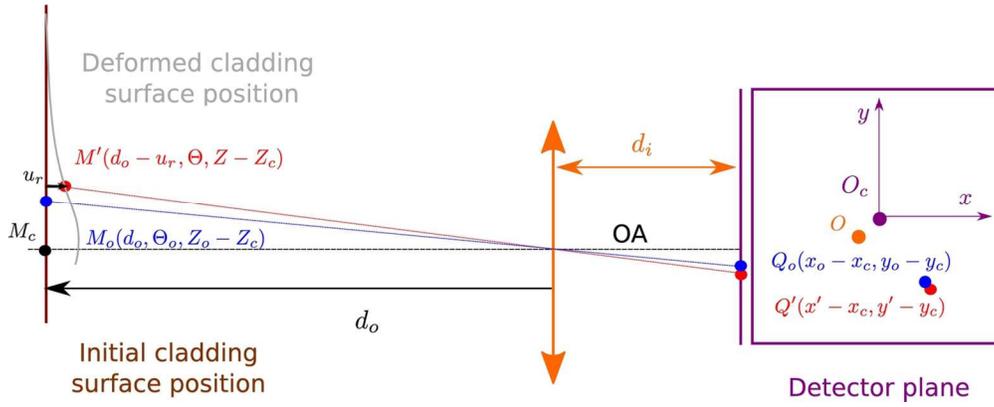
FIG. 9: Procedure Test B. Scheme of the combined edge detection / 2D-DIC approach.

131x52mm (300 x 300 DPI)
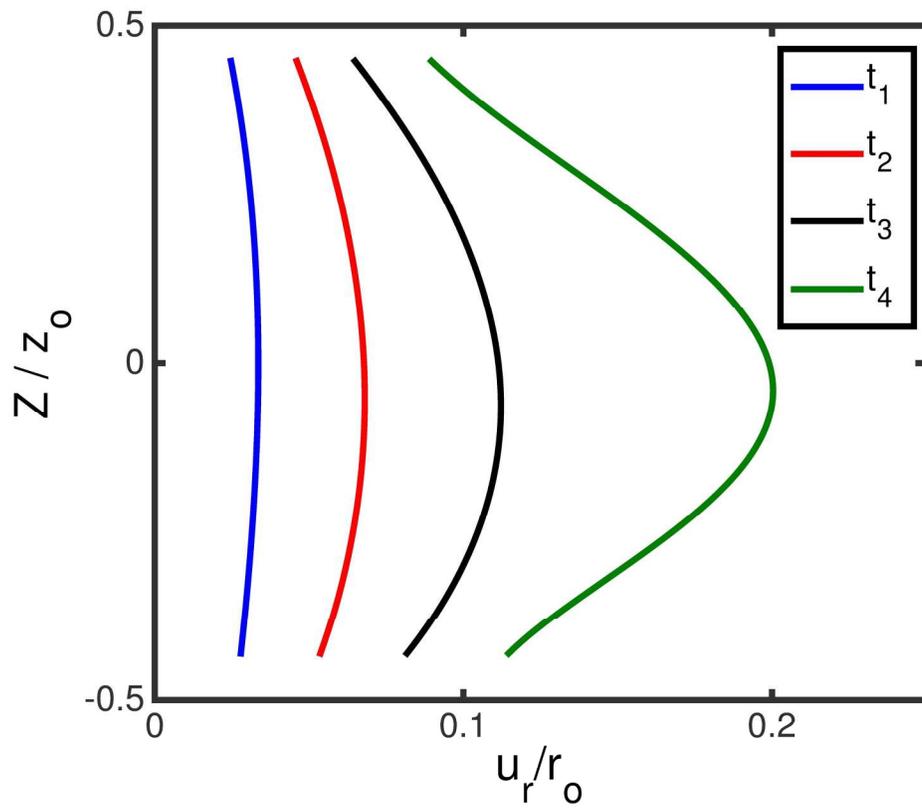
FIG. 10: Procedure Test B. Normalized out-of-plane displacement u_r/r_0 of each marker versus the normalized axial coordinate Z/Z_0
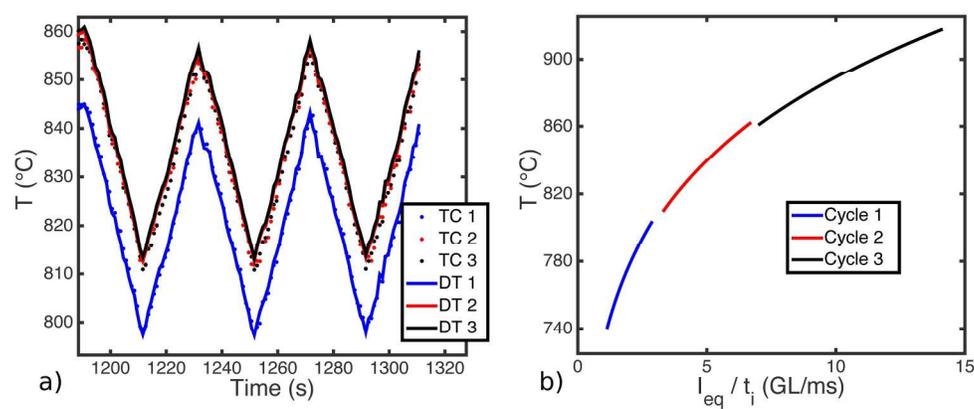
190x158mm (300 x 300 DPI)

FIG. 11: Procedure Test A a) Comparison NIRT – Thermocouples measurements for the second cycle of Test A. b) Radiometric model identification – one model per thermal cycle.
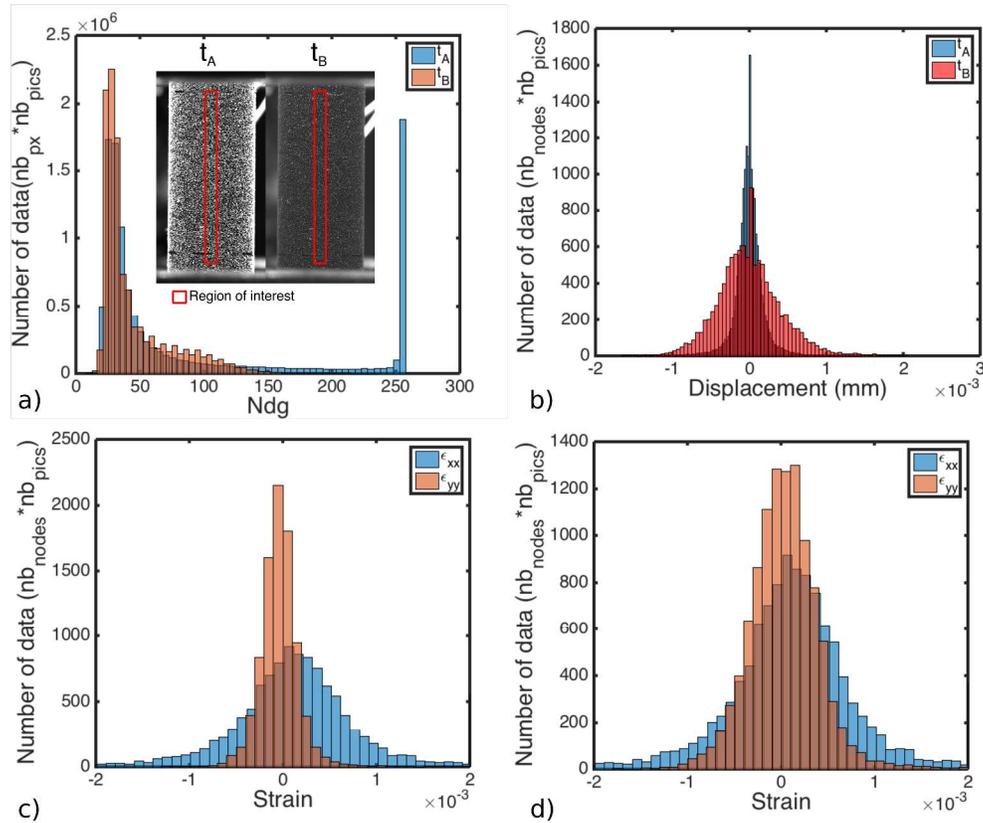
197x85mm (300 x 300 DPI)

FIG. 12: Procedure Test B. a) Grey level histograms of the sets of pictures associated to markers tA and tB, respectively at room and high temperature (See Fig. 4). b) Displacement histograms of the sets of pictures associated to markers tA and tB. c) Axial (εyy) and hoop Strains (εxx) histograms related to marker tA. d) Axial (εyy) and hoop Strains (εxx) histograms related to marker tB.
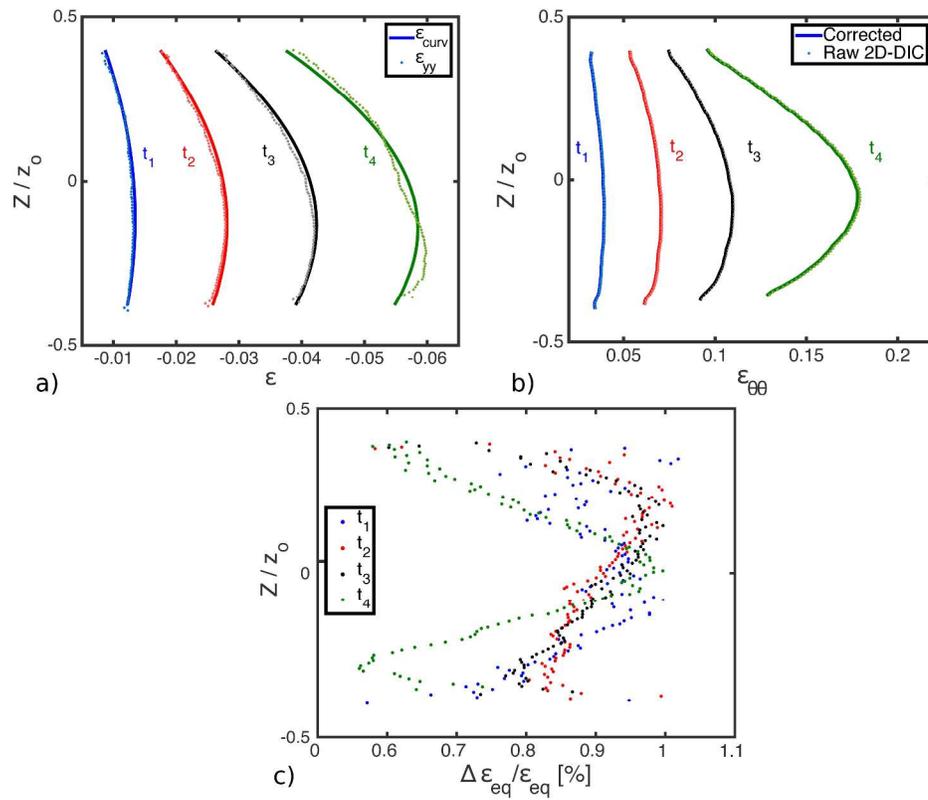
381x317mm (300 x 300 DPI)

FIG. 13: Comparison between the 2D-DIC and the combined edge detection / 2D-DIC approach, (a) axial strain, (b) hoop strain, (c) J2 equivalent strain.

381x310mm (300 x 300 DPI)